CLASH-VLT: Constraining deviation from GR with the mass profiles of nine massive galaxy clusters

Journal of Cosmology and Astroparticle Physics
An IOP and SISSA journal

Received: *September 23, 2025*
Revised: *December 11, 2025*
Accepted: *January 13, 2026*
Published: *March 6, 2026*

CLASH-VLT: Constraining deviation from GR with the mass profiles of nine massive galaxy clusters

L. Pizzuti,[a,b,*] **A. Biviano**,[b,c] **K. Umetsu**,[d] **E. Agostoni**,[a] **A. Autorino**,[a] **A. M. Pombo**,[e] **A. Mercurio**[f,g,h] **and M. D'Addona**[g]

[a] *Dipartimento di Fisica G. Occhialini, Università di Milano-Bicocca, Piazza della Scienza 3, 20126 Milano, Italy*
[b] *INAF-Osservatorio Astronomico di Trieste, via G. B. Tiepolo 11, 34143 Trieste, Italy*
[c] *IFPU-Institute for Fundamental Physics of the Universe, via Beirut 2, 34014 Trieste, Italy*
[d] *Academia Sinica Institute of Astronomy and Astrophysics (ASIAA), No. 1, section 4, Roosevelt Road, Taipei 106216, Taiwan*
[e] *CEICO, Institute of Physics of the Czech Academy of Sciences, Na Slovance 2, 182 21 Praha 8, Czech Republic*
[f] *Università di Salerno, Dipartimento di Fisica "E.R. Caianiello", Via Giovanni Paolo II 132, 84084 Fisciano (SA), Italy*
[g] *INAF Osservatorio Astronomico di Capodimonte, Salita Moiariello 16, 80131 Napoli, Italy*
[h] *INFN-Gruppo Collegato di Salerno-Sezione di Napoli, Dipartimento di Fisica "E.R. Caianiello", Università di Salerno, Via Giovanni Paolo II, 132, 84084 Fisciano (SA), Italy*

E-mail: lorenzo.pizzuti@unimib.it, andrea.biviano@inaf.it, keiichi@asiaa.sinica.edu.tw, e.agostoni6@campus.unimib.it, a.autorino1@campus.unimib.it, pombo@fzu.cz, amercurio@unisa.it, maurizio.daddona@inaf.it

Abstract: We investigate the anisotropic stress parameter, $\eta = \Psi/\Phi$, defined as the ratio of the gravitational potentials in the linearly perturbed Friedmann-Lemaître Robertson-Walker metric, as a probe of deviations from general relativity across astrophysical to cosmological scales. Using mass profiles reconstructed from high-precision lensing and kinematics of nine galaxy clusters from the CLASH-VLT sample, we derive $\eta(r)$ as a function of the radial distance from the cluster centres, over the range $[0.1\,\mathrm{Mpc}, 1.2\,r^L_{200}]$, where r^L_{200} is virial radius best-fit from lensing data. When using a Navarro-Frenk-White or an Hernquist profile to model the total matter distribution, we find consistency with general relativity ($\eta = 1$) within 2σ for the full radial range for all the sampled clusters. However, adopting a Burkert profile introduces mild tension with general relativity, reaching the 3σ level in two systems.

*Corresponding author.

https://doi.org/10.1088/1475-7516/2026/03/022

JCAP03(2026)022

Assuming a negligible time-dependence in the redshift range spawned by the clusters, we obtain the joint constraint $\eta(r = 1.0\,\mathrm{Mpc}) = 0.93^{+0.48}_{-0.40}$ (stat) ± 0.47 (syst) at 95% confidence level — an improvement of approximately 40% over previous estimates. We discuss the impact of systematics on the constraints, and we highlight the implications of this result for current and upcoming cluster surveys.

Keywords: galaxy clusters, gravitational lensing, gravity, modified gravity

ArXiv ePrint: 2509.16317

JCAP03(2026)022

Contents

1 Introduction

The discovery of the Universe's accelerated expansion (e.g. ref. [1, 2]), more than two decades ago, remains one of the most profound mysteries in modern cosmology. The current best description of a large variety of independent cosmological phenomena across different scales (e.g. ref. [3]) is the ΛCDM model. In this scenario, the observed acceleration is attributed to a cosmological constant, Λ, present in the field equations of Einstein's General Relativity (GR). However, the physical origin of this constant remains unknown (e.g. ref. [4, 5]).

Recent observations on both large and small scales have increasingly highlighted tensions between the predictions of the ΛCDM model and empirical data, as well as discrepancies among independent datasets. Notable examples include the S_8 tension (e.g. ref. [6, 7]), the CMB anisotropy anomalies (e.g. ref. [8, 9]), the 5σ Hubble tension (e.g. ref. [10]) between the high-redshift estimates of H_0 from the Cosmic Microwave Background (CMB) data (e.g. ref. [11]) and local measurements based on distance indicators (e.g. ref. [12]). Additionally, recent analyses combining DESI and CMB data indicate a time-dependent equation of state for Dark Energy (DE) (e.g. ref. [13]).

However, whether these tensions arise from an unknown systematic effect or signal the need for new physics beyond the ΛCDM model remains an open question. Nevertheless, the increasingly complex observational landscape has motivated the exploration of alternative models to the standard cosmological framework. Over the last 20 years, many theoretical models have been proposed to address these tensions. In addition to addressing these discrepancies, such models often seek to offer a more fundamental understanding of the nature of dark matter (DM) and DE components — introduced in ΛCDM to account for observations — which together constitute approximately 95% of the Universe's total energy/matter budget.

JCAP03(2026)022

A possible solution is to extend the ΛCDM model by introducing new interactions within the dark sector (DE+DM) or incorporating exotic fields characterized by non-standard equations of state. Among the various proposed possibilities, particular interest has been given to Modified Gravity (MG) theories (e.g. ref. [14]), in which GR is modified to mimic the effect of the dark sector at large scales in order to reproduce observations.

Whether by modifying gravity or redefining the physics of the dark sector, viable extensions to the ΛCDM model inevitably introduce new degrees of freedom that influence the formation and evolution of cosmic structures. Galaxy clusters - the largest structures in the Universe that have undergone gravitational collapse — are an excellent target of cosmological studies. Most of the matter content in clusters (roughly 85%) is understood to be in the form of invisible collisionless DM (e.g. ref. [15, 16]). While processes involving ordinary (baryonic) matter play a central role in the core of these structures, the overall cluster's dynamics is dominated by the gravitational interaction, making them ideal laboratories for investigating deviations from GR and probing the properties of the dark sector. Their internal mass distribution is dependent on the underlying cosmology, and they further probe both the relativistic and non-relativistic sectors of the gravitational interaction, through lensing and internal kinematics (of gas or member galaxies), respectively. For this purpose, galaxy clusters have been extensively used to test MG models through their mass profile reconstruction (with kinematics or lensing techniques, e.g. ref. [17]), abundance and spatial distribution (e.g. ref. [18, 19]).

One way to parametrize generic departures from standard gravity is to study the anisotropic stress η — *aka* gravitational slip. η is defined as the ratio between the relativistic and non-relativistic gravitational potentials, Ψ/Φ, that are components of the linearly perturbed Friedmann-Lemaitre-Robertson-Walker (FLRW) metric. In GR, and in models where additional degrees of freedom are minimally coupled to gravity, $\eta = 1$; this is no longer true in a general MG scenario. Here and in the following we further assume that DM is pressureless, and its contribution to the anisotropic stress tensor is negligible. Thus, a genuine departure from $\eta = 1$ can be linked to a departure from GR (e.g. ref. [20]).

In this work, we constrain η by using precise determinations of cluster mass profiles obtained from gravitational lensing and kinematic analyses of member galaxies. While galaxies move under the influence of the non-relativistic potential, Φ, photons propagate along null geodesics, reflecting the contribution of both relativistic, Ψ, and non-relativistic potentials, $\Phi_{\rm lens} = (\Psi + \Phi)/2$. A proper combination of lensing and kinematics mass estimates of clusters can thus be used to probe deviations from GR, under the assumption that possible systematic effects are under control.

Through a similar approach to the one in ref. [17], we compute the radial profile $\eta(r)$ in the region $r > 0.1\,$Mpc for nine clusters. These nine clusters were chosen based on the availability of high-precision imaging and spectroscopic data obtained from the Cluster Lensing and Supernova Survey with Hubble (CLASH) collaboration, along with its follow-up observations using the VIMOS spectrograph at the Very Large Telescope (CLASH-VLT). The kinematic mass profiles were reconstructed by analysing the positions and line-of-sight velocities of cluster members with the MG-MAMPOSSt code (e.g. ref. [21]). We then combined these results with the strong+weak gravitational lensing posteriors from ref. [22]. In our analysis, we explore various models for both lensing and kinematic mass profiles, while

JCAP03(2026)022

also addressing the impact of systematics. A particular focus is placed on deviations from spherical symmetry and the equilibrium configuration.

The paper is structured as follows: section 2 reviews the definition of the anisotropic stress and its connection to the clusters' total mass profiles; in section 3, we present the dataset, further elaborating on the kinematic mass reconstruction with MG-MAMPOSSt. Section 4 is devoted to the main results, which are further summarised in section 5.

Throughout this paper, we assume a flat ΛCDM cosmology with $H_0 = 70$ km s^{-1} Mpc^{-1}, $h = H_0/(100$ km s^{-1} Mpc$^{-1})$, $\Omega_m = 0.3$, $\Omega_\Lambda = 0.7$.

2 Theoretical background

While galaxy clusters are highly non-linear perturbations of the matter density field, their geometry can still be described by a linear perturbation of the FLRW metric (e.g. ref. [17]). In the conformal Newtonian gauge, the line element reads:

$$\mathrm{d}s^2 = -\left(1 + \frac{2\,\Phi}{c^2}\right) c^2 \mathrm{d}t^2 + a^2(t) \left(1 - \frac{2\,\Psi}{c^2}\right) \left[\mathrm{d}r^2 + r^2 \mathrm{d}\Omega^2\right] , \tag{2.1}$$

where $\Phi(t, \vec{x})$ and $\Psi(t, \vec{x})$ are the two gauge-invariant non-relativistic and relativistic potentials, respectively. In GR, for a fluid with a negligible anisotropic stress-energy tensor, one has $\Phi = \Psi$ at all points in spacetime, a relation valid up to second-order corrections ($\ll 1$) in the relativistic expansion of the potentials. Assuming such a configuration, generic departures from standard gravity can be quantified with the anisotropic stress $\eta = \Psi/\Phi$, which is a general function of scale and time and whose specific form depends on the assumed model. Following the work done in ref. [17, 23], we employ a phenomenological, nearly model-independent determination of $\eta(r, t)$ using the mass profiles of galaxy clusters derived from kinematic and lensing analysis. The dependence on the scale is encapsulated in the free parameters of the mass density profiles.

Under the assumption of dynamical relaxation, member galaxies in clusters move smoothly under the non-relativistic potential, Φ, and follow the Jeans' equation:

$$\frac{\mathrm{d}(\nu\sigma_r^2)}{\mathrm{d}r} + 2\beta(r)\frac{\nu\,\sigma_r^2}{r} = -\nu(r)\,\frac{\mathrm{d}\Phi}{\mathrm{d}r} , \tag{2.2}$$

where we have further assumed spherical symmetry; $\nu(r)$, is the number density profile of tracers, as a function of the 3-dimensional radial distance from the cluster center; σ_r^2, is the velocity dispersion along the radial direction, and $\beta \equiv 1 - (\sigma_\theta^2 + \sigma_\varphi^2)/2\sigma_r^2$ is the so called velocity anisotropy. The σ_θ^2 and σ_φ^2 are the velocity dispersion components along the tangential and azimuthal directions, respectively. Spherical symmetry imposes $\sigma_\theta^2 = \sigma_\varphi^2$ and the expression of the anisotropy profile simplifies to $\beta = 1 - \sigma_\theta^2/\sigma_r^2$.

The gradient of the potential is connected to the total (effective) dynamical mass through the Poisson equation,

$$\frac{\mathrm{d}\Phi}{\mathrm{d}r} = \frac{G M_{\rm dyn}(r)}{r^2} , \tag{2.3}$$

where

$$M_{\rm dyn}(r) = 4\pi \int_0^r r'^2\, \rho_{\rm dyn}(r')\, \mathrm{d}r' , \tag{2.4}$$

JCAP03(2026)022

with $\rho_{\rm dyn}(r)$ the effective dynamical density.[1]

Concerning the lensing mass, we can derive a similar expression by considering that photon propagation is affected by both relativistic and non-relativistic potentials. The potential experienced by photons — the source of gravitational lensing, commonly referred to as the Weyl potential (e.g. ref. [24]) — is defined as $\Phi_{\rm lens} = (\Phi + \Psi)/2$, which satisfies the analogous of eq. (2.3) for an effective lensing mass,

$$\frac{{\rm d}(\Phi + \Psi)}{{\rm d}r} = 2\,\frac{G M_{\rm lens}(r)}{r^2}\,. \tag{2.5}$$

The resulting anisotropic stress comes as

$$\eta(r) = \frac{\int_r^\infty \left[2M_{\rm lens}(r') - M_{\rm dyn}(r')\right]\frac{{\rm d}r'}{r'^2}}{\int_r^\infty M_{\rm dyn}(r')\frac{{\rm d}r'}{r'^2}}\,. \tag{2.6}$$

2.1 Mass modeling

In this work, we adopt three different models to describe the total effective mass profiles of the clusters under analysis. The models were chosen such that they provide adequate fits for both kinematics and lensing data (see section 3). All models are characterized by two free parameters: the "virial" radius r_{200}, which is the radius of a sphere enclosing an average density 200 times the critical density of the Universe at the cluster's redshift; and a scale radius $r_{\rm s}$, characterizing the change of slope from the inner to the outer part of the matter distribution. The first model to consider is the popular Navarro-Frenk-White (NFW) profile (e.g. ref. [25]) is given by

$$M_{\rm NFW}(r) = M_{200}\frac{\ln(1 + r/r_{\rm s}) - \frac{r/r_{\rm s}}{(1+r/r_{\rm s})}}{\ln(1 + r_{200}/r_{\rm s}) - \frac{r_{200}/r_{\rm s}}{(1+r_{200}/r_{\rm s})}}\,, \tag{2.7}$$

where $r_{\rm s} \equiv r_{-2}$ is the radius at which the logarithmic derivative of the density profile is -2.

The second is the Burkert model (e.g. ref. [26]), defined as

$$M_{\rm Bur}(r) = M_{200}\frac{\ln[1 + (r/r_{\rm s})^2] + 2\ln(1 + r/r_{\rm s}) - 2\arctan(r/r_{\rm s})}{\ln[1 + (r_{200}/r_{\rm s})^2] + 2\ln(1 + r_{200}/r_{\rm s}) - 2\arctan(r_{200}/r_{\rm s})}\,, \tag{2.8}$$

where $r_{\rm s} \simeq 2/3\, r_{-2}$. Finally, we consider the Hernquist model profile (e.g. ref. [27]),

$$M_{\rm Her}(r) = M_{200}\frac{(r_{200} + r_{\rm s})^2}{r_{200}^2}\frac{r^2}{(r + r_{\rm s})^2}\,, \tag{2.9}$$

with $r_{\rm s} = 2\, r_{-2}$. Note that, while the NFW and Hernquist models have a central density which diverges as r^{-1}, the Burkert model exhibits a core. For all three models, analytical expressions of $\eta(r)$ can be derived by integrating the total mass as in eq. (2.6). In the following, we compute the anisotropic stress using the profile models to account for possible systematics arising from the parametrization of the total cluster mass. For our reference analysis, we adopt the NFW model, which has been shown to provide the best fit of the stacked lensing signal from the analysis of ref. [22].

[1]The term "effective" indicates that $\rho_{\rm dyn}(r)$ may include contributions coming from additional degrees of freedom in theories beyond ΛCDM, which are not explicitly modeled.

JCAP03(2026)022

3 Dataset and mass profiles

Our target is a sample of nine massive galaxy clusters, namely: Abell 383 (A383), Abell 209 (A209), RX J2129.7+0005 (R2129), MS2137−2353 (MS2137), RXC J2248.7−4431 (R2248, also named Abell S1063), MACS J1931.8−2635 (M1931), MACS J1115.9+0129 (M1115), MACS J1206.2−0847 (M1206), and MACS J0329.7−0211 (M329), spanning the redshift range $0.18 < z \leq 0.45$. The sample has been extensively studied within the CLASH (*e.g.* ref. [28]) and CLASH-VLT (e.g. ref. [29]) collaborations. The full CLASH sample comprises twenty-five galaxy clusters, of which twenty were selected for their high X-ray temperatures ($kT_{\rm X} > 5\,{\rm keV}$) and morphologically regular X-ray appearance, as observed with *Chandra*. The two-dimensional weak-lensing analysis of [30] clearly detected the elliptical shapes of cluster halos at a significance of 5σ in a sample of 20 CLASH clusters. However, the measured ellipticity for the CLASH sample shows a mild 1σ hint of rounder halo shapes relative to the ΛCDM prediction. The degree of dynamical relaxation in this sample - a fundamental assumption for the analysis presented here - will be further examined below.

For our nine clusters, deep wide-field multi-band imaging was obtained and analyzed as part of the CLASH program, as presented in ref. [31]. For eight clusters (excluding R2248), the multi-band photometry was acquired with Suprime-Cam (e.g. ref. [32]) on the 8.2 m Subaru Telescope. For R2248, the imaging was instead obtained with the Wide-Field Imager on the 2.2 m MPG/ESO telescope at La Silla, as reported by ref. [33]. We refer the reader to ref. [31] for full details.

As for the spectroscopic information, essential for the kinematic analysis, the main source of spectroscopic data for the nine clusters is the CLASH-VLT program (e.g. ref. [29]), based on observations taken with the VIsual Multi-Object Spectrograph (VIMOS; e.g., ref. [34]), and with the Multi Unit Spectroscopic Explorer (MUSE; e.g. ref. [35]), at the Very Large Telescope. MUSE observations are available for eight of the nine clusters, with the exception of MS2137.

3.1 Lensing mass profiles

In this work, we derive marginalized posterior distributions for the (r_{-2}, r_{200}) parameters of our nine CLASH clusters, using the combined weak and strong-lensing data products presented in ref. [22], assuming the three mass profile models introduced in section 2.1. To this end, we use the piecewise-defined convergence profiles and total covariance matrices obtained by ref. [22] for the CLASH clusters (see their appendix B). In the lensing analysis, the total covariance matrix accounts for multiple sources of uncertainty (see ref. [36]), including statistical measurement errors, systematic effects primarily due to the residual mass-sheet degeneracy, the cosmic noise covariance from uncorrelated large-scale structures projected along the line of sight, and intrinsic variations in the lensing signal at fixed halo mass arising from halo triaxiality and projection effects.

For all models, we adopt uninformative, log-uniform priors on both the halo mass, M_{200}, and the halo concentration, $c_{200} \equiv r_{200}/r_{-2}$, with prior ranges defined as $M_{200} \in [10^{14}, 10^{16}]\, h^{-1}\, M_{\odot}$ and $c_{200} \in [1, 20]$. For each cluster and each mass model, we then infer the posterior probability distribution in the (r_{-2}, r_{200}) parameter space. The resulting parameter constraints are summarized in the third and fourth columns of table 1.

JCAP03(2026)022

3.2 Kinematic mass reconstruction

The kinematic mass profiles are derived by means of the MG-MAMPOSSt code (e.g. ref. [21, 37]), a version of the MAMPOSSt method of ref. [38] which jointly reconstructs the velocity anisotropy and the mass profiles of clusters[2] using data of projected position, R, and line-of-sight velocities, v_z, in the cluster rest-frame, for cluster members. The points (R, v_z) define the projected phase-space (p.p.s. hereafter).

In this work, we employ the same setup as in Ref. [39]; in particular, we consider the members selected in there by the application of the CLUster Membership in Phase Space (CLUMPS) method of ref. [40], further refined by ref. [39].

For each cluster, we consider galaxies up to a projected radius $R = r_{200}^L$, where r_{200}^L is the value of the virial radius estimated by the lensing analysis of ref. [30]. This choice limits the MG-MAMPOSSt analysis to a region in which the Jeans equation is more reliably applied, given that external cluster regions are less likely to be in dynamical equilibrium.

As we have done in previous works (see e.g. ref. [41, 42]), we checked that a variation of $\sim 10\%$ of this limit does not produce relevant effects on the final results. As for the lower limit, we excluded the central region $R < 0.05\,\mathrm{Mpc}$ where the total mass profile and the dynamics is strongly influenced by the brightest cluster galaxy (BCG) that dominates the gravitational potential (e.g. ref. [16, 43]).

Assuming that the 3-dimensional velocity distribution of member galaxies is Gaussian, the MG-MAMPOSSt procedure solves the Jeans equation to obtain the radial velocity dispersion $\sigma_r^2(r)$ for a set of parameters describing the mass profile $M(r)$, the velocity anisotropy profile, $\beta(r)$, and the number density $\nu(r)$. The radial dispersion is then projected along the line-of-sight. The code computes the probability $q(R, v_z|\vec{\theta})$ of finding a galaxy at the point (R, v_z) of the phase space, given the set of parameters $\vec{\theta}$. The MG-MAMPOSSt log likelihood is then given by

$$\ln \mathcal{L}_{MAM}(\vec{\theta}) = \sum_{i=1}^{N} \ln \left[q(R^{(i)}, v_z^{(i)}|\vec{\theta}) \right], \tag{3.1}$$

where the sum runs over the N galaxies in the p.p.s.

For the Jeans analysis, we consider the generalized Tiret model for the velocity anisotropy profile (e.g. ref. [44, 45]),

$$\beta_{gT}(r) = \beta_0 + (\beta_\infty - \beta_0)\frac{r}{r + r_\beta}\,, \tag{3.2}$$

where β_0 and β_∞ represent the anisotropy at $r = 0$ and at very large radii, $r \gg r_\beta$, respectively. r_β is a scale radius which is usually set to be equal to r_{-2} of the cluster mass profile. In this work, we also explore the possibility of keeping r_β as an additional free parameter; we further consider a different model of velocity anisotropy, the Pizzuti & Biviano profile, or exponential Tiret (BP hereafter, see Maraboli et al., in prep.),

$$\beta_{BP}(r) = \beta_0 + (\beta_\infty - \beta_0)\left[\frac{r}{r + r_\beta} + \frac{r^2}{r_\beta^2} e^{-\left(\frac{r}{r_\beta}\right)^2}\right], \tag{3.3}$$

[2]Note that in general, the algorithm can be applied to any auto-gravitating system of particles moving smoothly under the influence of a gravitational potential.

JCAP03(2026)022

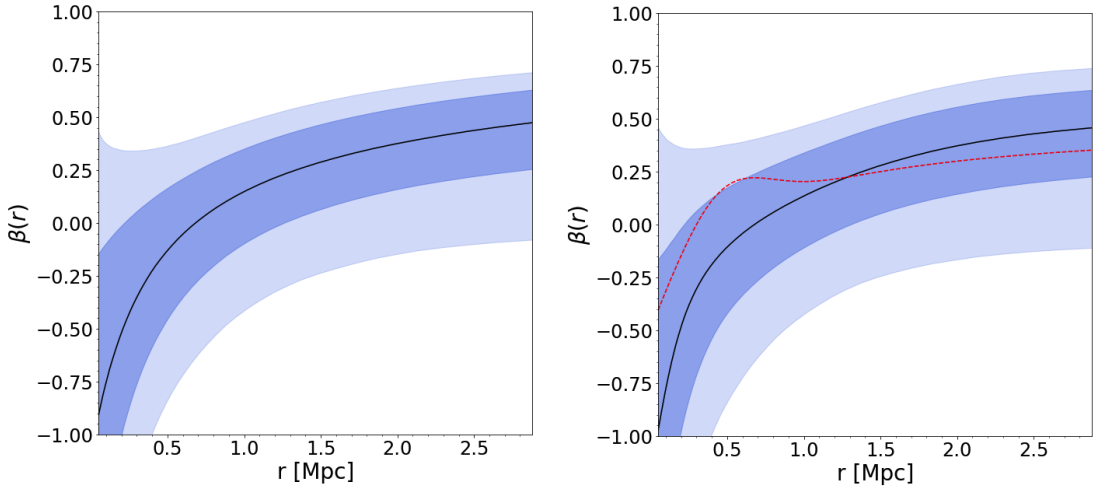

Figure 1. Anisotropy profiles of the cluster A209 reconstructed from the kinematic analysis with the MG-MAMPOSSt method Left: gT model. Right: BP model. In both cases, a NFW mass profile has been used. The darker and lighter shaded regions indicate 1 and 2 σ limits, respectively. The red dashed line in the plot on the right shows a BP profile with $\beta_0 = -0.5$, $\beta_\infty = 0.5$ and $r_\beta = 0.5\,\mathrm{Mpc}$, for the only illustrative purpose of highlighting the features of the PB model.

which allows for a bump in the velocity anisotropy at $r \sim r_\beta$.

Both gT and BP models are general enough to capture quite a broad range of orbit phenomenology for galaxies in clusters.MG-MAMPOSSt works using the scaled anisotropy parameters, $\mathcal{A}_0, \mathcal{A}_\infty$, defined as $\mathcal{A}_{0/\infty} = (1-\beta_{0/\infty})^{-1/2}$. Radial (tangential) orbits correspond to $\mathcal{A} > 1$ (< 1, respectively), and $\mathcal{A} = 1$ corresponds to isotropic orbits ($\beta = 0$).

In figure 1 we plot an exemplary case of the anisotropy profiles. This corresponds to the A209 cluster obtained by means of the MG-MAMPOSSt procedure, assuming a gT model (left) and the BP model (right). The resulting profiles are almost identical within the errors. We also plot a BP model with $\beta_0 = -0.5$, $\beta_\infty = 0.5$, and $r_\beta = 0.5\,\mathrm{Mpc}$ (red dashed line in the right plot) to highlight the features of this new model. The similarity of the gT and PB profiles indicates that the additional feature in the PB model with respect to the gT model does not provide an improved representation of the cluster $\beta(r)$.

The last ingredient needed for the kinematic analysis is the number density profile of the galaxies. This can be obtained by fitting the radial density distribution $N(R)$ in projection, after correcting for the completeness of the sample, before running the MG-MAMPOSSt procedure. Note that only the scale radius r_ν of the profile is required in the Jeans analysis, as the normalization simplifies in the expression of $\sigma_r^2(r)$. Here, we rely on the results of ref. [39], where the projected NFW (pNFW) model (e.g. ref. [46]) and the King profile (e.g. ref. [47]) are fitted to the p.p.s. with the method of ref. [48], which doesn't require binning of the data. The pNFW model provides a better fit than the King model for all clusters except for the A209; the constraints on r_ν with the $1\,\sigma$ uncertainties are listed in column 7 of table 1.

JCAP03(2026)022

To account for variability in the number density scale radius, r_ν is treated as a free parameter in MG-MAMPOSSt, with a Gaussian prior whose standard deviation corresponds to the 68% confidence interval from the external fit.

For each cluster, we perform a Monte-Carlo Markov-Chain (MCMC) sampling of the likelihood distribution of (3.1) for 110 000 points in the parameter space. We discard the first 10 000 points as a burn-in phase. As done in previous works (e.g., ref. [42]), the convergence is ensured by running 5 chains for every model choice and checking that the condition for the Geller-Rubin coefficient $\hat{R} < 1$ is satisfied.

We consider un-informative, flat priors in $r_{200} \in [0.3, 5.0]\,\mathrm{Mpc}$, $r_s, r_\beta \in [0.05, 4.0]\,\mathrm{Mpc}$, $\mathcal{A}_{0/\infty} \in [0.5, 7.0]$; for r_ν the above mentioned Gaussian prior is assumed. The resulting $1\,\sigma$ and $2\,\sigma$ posterior distributions in the r_{200}-r_{-2} space are shown for each cluster in appendix A, adopting the reference model gT for $\beta(r)$, compared to the lensing posteriors of ref. [22].

A visual inspection of figures 7, 8, 9, reveals that the kinematic reconstruction exhibits little variation when changing the mass model in the MG-MAMPOSSt procedure, differently from the lensing case. This confirms the robustness of the kinematic analysis against different choices of the total mass profile. This is further indicated by the fact that the value of $\Delta\chi^2 = -2\Delta(\ln \mathcal{L}_{MAM})$ among the three models is always smaller than 1.0. An exemption occurs for the R2129 for which the NFW profile is mildly preferred with a $\Delta\chi^2 \gtrsim 3$.

However, some clusters show a mild ($\lesssim 2\sigma$) tension between the lensing and kinematic distributions, as one can visually determine again from figures 7, 8 and 9; and by comparing the values listed in columns 3 and 4 of table 1 with the corresponding values in columns 5 and 6, where we report the MG-MAMPOSSt constraints on r_{200} and r_s for the NFW+gT case.

The shift is evident in the scale radius of A209 and in the virial radius of M1115, where the kinematic analysis predicts systematically lower values of r_s and r_{200}, respectively, with respect to the lensing case. The opposite trend is instead found for R2248, with overall larger dynamical masses. While M1115 does not exhibit strong evidence of unrelaxation (e.g. ref. [49]), A209 may have undergone (or is currently undergoing) a merging event, see ref. [50] and references therein. As for R2248, an indication of an off-axis merging event has been found by ref. [51], suggesting that the cluster is not dynamically relaxed. We marked in bold these clusters in table 1.

It is also worth pointing out the slight tension in M1206, which was not found in the case study of ref. [17]. In this, full consistency was shown between the kinematic and lensing profiles. As explained in ref. [43], the new p.p.s. membership selection, based on the CLASH-VLT+MUSE data, has been able to identify a foreground group which is located close to $R = 0$ in projection, and which therefore is not considered in the MG-MAMPOSSt run. However, this substructure has not been excluded in the strong+weak lensing analysis of ref. [22], producing a slight disagreement between the two mass determinations.

4 Results

We reconstruct $\eta(r)$ by applying eq. (2.6) as follows: we consider 10^5 arrays of parameters $(r^L_{200}, r^L_s, r^D_{200}, r^D_s)$, randomly extracted from the MCMC samples of the lensing and kinematic posterior distributions. We then compute $\eta(r)$ in the radial range $[\,0.1\,\mathrm{Mpc},\, 1.2\,r^L_{200}\,]$, where r^L_{200} is the best fit value of r_{200} found by the lensing analysis of ref. [22]. The lower limit is

JCAP03(2026)022

Cluster	z	r_{200}^{L}	r_{s}^{L}	r_{200}^{D}	r_{s}^{D}	r_{ν}	N_{200}	A^2	f_{sub}
A383	0.187	$1.78^{+0.43}_{-0.41}$	$0.33^{+0.30}_{-0.24}$	$1.79^{+0.15}_{-0.14}$	$0.23^{+0.24}_{-0.19}$	$0.47^{+0.08}_{-0.07}$	425	0.65	0.20
A209	**0.209**	$\mathbf{2.33^{+0.39}_{-0.41}}$	$\mathbf{1.02^{+0.66}_{-0.56}}$	$\mathbf{2.39^{+0.17}_{-0.16}}$	$\mathbf{0.61^{+0.54}_{-0.43}}$	$\mathbf{0.66^{+0.03}_{-0.04}}$	**864**	**0.75**	**0.40**
R2129	0.234	$1.62^{+0.32}_{-0.31}$	$0.31^{+0.25}_{-0.20}$	$1.48^{+0.44}_{-0.54}$	$1.46^{+2.13}_{-1.51}$	$1.02^{-0.21}_{+0.26}$	185	0.36	0.46
MS2137	0.313	$2.02^{+0.50}_{-0.56}$	$0.83^{+0.92}_{-0.72}$	$1.49^{+0.38}_{-0.50}$	$0.91^{+2.05}_{-0.97}$	$1.09^{+0.33}_{-0.25}$	140	0.75	0.47
R2248	**0.348**	$\mathbf{2.25^{+0.54}_{-0.51}}$	$\mathbf{0.72^{+0.77}_{-0.55}}$	$\mathbf{2.52^{+0.24}_{-0.22}}$	$\mathbf{0.72^{+0.62}_{-0.49}}$	$\mathbf{0.97^{+0.10}_{-0.09}}$	**688**	**1.02**	**0.50**
M1931	0.352	$2.27^{+0.67}_{-0.66}$	$0.78^{+1.03}_{-0.69}$	1.93 ± 0.30	$0.64^{+1.16}_{-0.66}$	$1.13^{+0.29}_{-0.23}$	218	0.20	0.10
M1115	**0.355**	$\mathbf{2.16^{+0.31}_{-0.34}}$	$\mathbf{0.77^{+0.48}_{-0.41}}$	$\mathbf{1.67^{+0.32}_{-0.36}}$	$\mathbf{1.36^{+1.69}_{-1.16}}$	$\mathbf{1.06^{+0.18}_{-0.14}}$	**363**	**0.67**	**0.31**
M1206	0.439	$2.15^{+0.32}_{-0.34}$	$0.62^{+0.45}_{-0.37}$	$2.02^{+0.16}_{-0.15}$	$0.28^{+0.33}_{-0.23}$	$0.67^{+0.10}_{-0.12}$	409	0.49	0.22
M329	0.450	$1.66^{+0.26}_{-0.27}$	$0.25^{+0.18}_{-0.15}$	$1.75^{+0.29}_{-0.35}$	$0.67^{+1.51}_{-0.68}$	$0.70^{+0.15}_{-0.13}$	199	0.40	0.0

Table 1. Summary of the constraints on r_{200} and r_s along with their 2σ uncertainties for the set of nine CLASH clusters analysed here. All radii are in Mpc units. We adopt the reference model NFW for both lensing and kinematic masses, with a gT model for the velocity anisotropy profile. First column: cluster denomination. Second column: redshift. Third and fourth columns: constraints from the lensing analysis of [22]. Columns five and six: constraints from MG-MAMPOSSt. Column seven: scale radius of the number density profile along with its 1σ uncertainties, adopted as Gaussian priors in the kinematic MCMC run. Column eight: number of selected members within r_{200}^{L}. Column nine: Anderson-Darling coefficient. Column ten: fraction of galaxies in substructures. We marked in bold the clusters with signs of an un-relaxed state.

chosen to exclude the central cluster region, where the uncertainties on the lensing model become larger (e.g. refs. [22, 52]) and the dynamics becomes more influenced by the BCG and baryonic processes. As indicated by hydrodynamical simulations, the competition between adiabatic contraction and AGN feedback can significantly alter the total mass profile in the core (e.g. refs. [53, 54]). Recent observational works on individual clusters support this complexity: for instance, a detailed multi-component kinematic analysis of M1206, ref. [43] - modeling gas, galaxies, and BCG dispersion - favoured a shallower dark matter profile compared to the NFW prediction. Conversely, the cluster R2248 was found to be consistent with the standard NFW model, ref. [16], though this might be related to its dynamical un-relaxation state. Furthermore, baryonic effects are known to bias lensing mass estimates in the central region of clusters (e.g. ref. [55]).

While a full multi-component approach combining lensing and kinematics would be ideal to disentangle these effects - a topic we are currently addressing in a separate work, Pizzuti et al., 2026, *in prep.* - it requires specific BCG data not uniformly available for our sample. However, to assess the impact of this choice on our results, we performed robustness tests by varying the lower radial cut of the $\eta(r)$ profile down to $r = 0\,\mathrm{Mpc}$. We found that the reconstructed $\eta(r)$ profiles do not show any significant difference in the extended radial range. This suggests that, given the current precision of the data, the systematic uncertainty introduced by baryonic modeling in the core is sub-dominant compared to the statistical errors.

As for the upper limit, note that extending the analysis beyond r_{200} is generally not appropriate, as the assumption of dynamical equilibrium may break down at such large radii. For the lensing data, parameter inference is limited to $r = 2\,h^{-1}\,\mathrm{Mpc} \simeq 2.9\,\mathrm{Mpc}$, beyond

JCAP03(2026)022

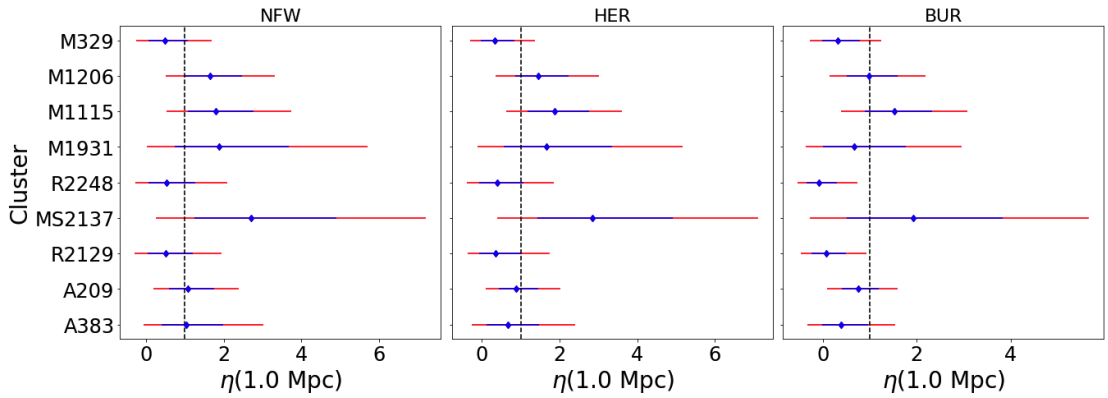

Figure 2. Constraints on $\eta(r = 1.0\,\mathrm{Mpc})$ for the nine clusters in the sample. In each plot, a gT model is assumed for the velocity anisotropy profile in the kinematic analysis. The blue segments refer to 68% C.L., while the red lines indicate the 95% C.L. For Left: NFW model. Middle: Hernquist model. Right: Burkert model. The black dashed vertical lines mark the GR expectation $\eta = 1$.

which the contribution from surrounding large-scale structure becomes increasingly significant (see figure 3 of ref. [22]). Keeping all of this in mind, we quoted as our reference value for each cluster $\eta(r = 1.0\,\mathrm{Mpc})$ as a fair trade-off between the upper and lower bounds. Note also that around $r \sim 1\,\mathrm{Mpc}$ the radial profiles $\eta(r)$ tend to flatten (see figure 11 of appendix B). Moreover, for many viable MG models, the innermost cluster region is totally screened, masking additional effects induced by departures from GR (see e.g. ref. [56]).

In figure 2 we plot the constraints of $\eta(r = 1.0\,\mathrm{Mpc})$ derived at 1σ and 2σ for all the clusters in the sample. Each plot corresponds to a different model of $M(r)$, while the gT profile is adopted for the velocity anisotropy in all cases. The full radial profiles of $\eta(r)$ for the reference model NFW+gT are also reported in figure 11 of appendix B.

Independently of the mass model assumed, the GR expectation $\eta = 1$ is always included within 2σ, except for the Burkert case, where two clusters (R2248 and R2129) exhibit a $\sim 3\sigma$ tension in favour of $\eta < 1$. Note, however, that the lensing analysis disfavors the Burkert model when compared to the other two profiles (see e.g. ref. [22]). In order to provide a more quantitative estimate of the relative performance of the three mass models, we compute the difference in log-evidence with respect to the NFW profile, $\Delta \ln Z = \ln Z_{\mathrm{model}} - \ln Z_{\mathrm{NFW}}$, ($Z$ being the evidence) for each cluster. For the Hernquist profile we find

$$\Delta \ln Z_{\mathrm{Her-NFW}} \in [\,-0.25,\ 1.66\,], \tag{4.1}$$

with typical values $|\Delta \ln Z| \lesssim 1$. According to the Jeffreys scale, this corresponds at most to weak evidence and indicates that, on a cluster-by-cluster basis, Hernquist and NFW provide statistically comparable descriptions of the data, with no strong preference for either profile. In contrast, the Burkert model is systematically disfavoured, yielding

$$\Delta \ln Z_{\mathrm{Bur-NFW}} \in [\,-5.98,\ -1.99\,],$$

with negative values for all systems. In particular, for the two clusters that also display the strongest tension in the anisotropic stress parameter, we obtain $\Delta \ln Z_{\mathrm{Bur-NFW}} = -3.69$, and

JCAP03(2026)022

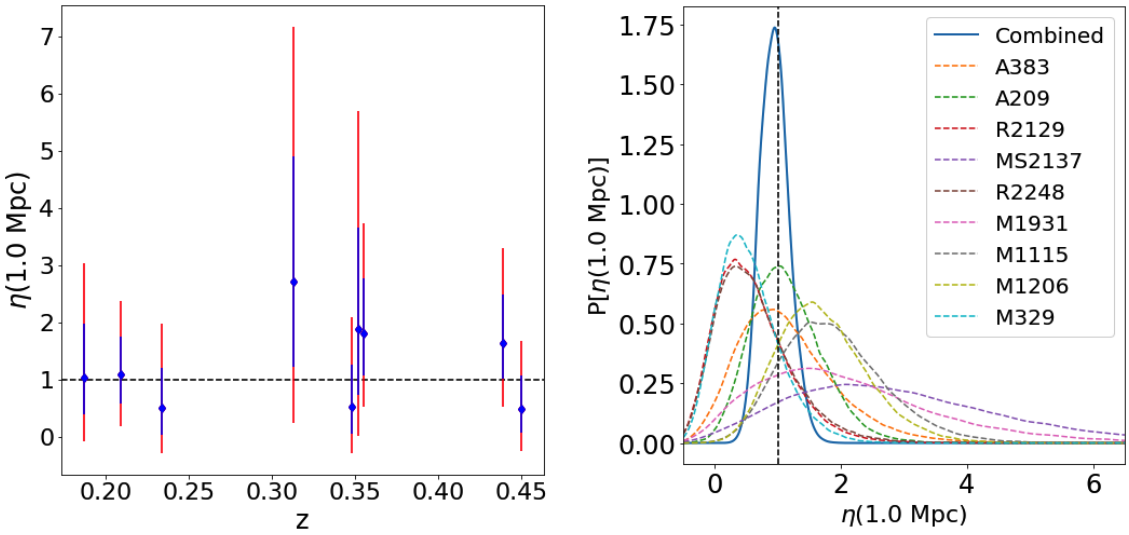

Figure 3. Left: constraints on $\eta(r = 1.0\,\mathrm{Mpc})$ as a function of the redshift for the NFW+gT model. The color code is the same as in figure 2. Right: Posterior distributions from the analysis of each single cluster (dashed lines), computed at $r = 1.0\,\mathrm{Mpc}$, and combined distribution (solid line).

-5.98 for R2129 and R2248, respectively, corresponding to Bayes factors of order $e^{|\Delta \ln Z|} \sim 40$–400 in favour of NFW over Burkert. According to the standard Jeffreys classification, this constitutes strong to very strong evidence against the Burkert profile. In summary, while NFW and Hernquist are essentially indistinguishable from the point of view of the Bayesian evidence, the Burkert profile is significantly disfavoured by our cluster sample, consistently with its poorer performance inferred from the lensing analysis alone. The individual constraints of $\eta(r = 1.0\,\mathrm{Mpc})$ are further shown in the second, fourth, and sixth columns of table 2, for NFW, Hernquist, and Burkert total mass profiles, respectively.

In the left panel of figure 3, we plot $\eta(r = 1.0\,\mathrm{Mpc})$ as a function of the cluster redshift z for the reference model NFW+gT. No evidence of time evolution has emerged from our analysis in the redshift range explored; this statement motivates the possibility of combining the single marginalized posterior distributions $P[\eta(r = 1\,\mathrm{Mpc})]$ to get the joint constraint on the anisotropic stress for our cluster sample. The distributions for all the clusters, as well as the combined posterior for the NFW+gT case, are plotted in the right panel of figure 3. The left panel of figure 4 shows the effect on the distribution of adopting different mass models in the analysis. While NFW and Hernquist profiles show similar results, in agreement with GR expectation $\eta = 1$ within 68% C.L. and 95% C.L., respectively, the Burkert ansatz provides a posterior significantly shifted towards $\eta < 1$. We find $\eta(r = 1.0\,\mathrm{Mpc}) = 0.93^{+0.22}_{-0.18}\,(1\sigma)\,^{+0.48}_{-0.40}\,(2\sigma) \pm 0.47\,(\mathrm{syst})$, where the systematic uncertainties reflect the variation of the peak of the distribution induced by the choice of the mass profile. In particular, we have considered the distances $\delta\eta^{(X)}_{\mathrm{max}} = \eta^{(NFW)}_{\mathrm{max}} - \eta^{(X)}_{\mathrm{max}}$, with $X = Bur, Her$, and $\eta^{(NFW,X)}_{\mathrm{max}}$ represents the value of η where the marginalized distribution exhibits the maximum. The largest $\delta\eta$ has been found for the Burkert case, $\delta\eta^{(Bur)}_{\mathrm{max}} = 0.47$, that we quote as our estimate of the systematic error.

JCAP03(2026)022

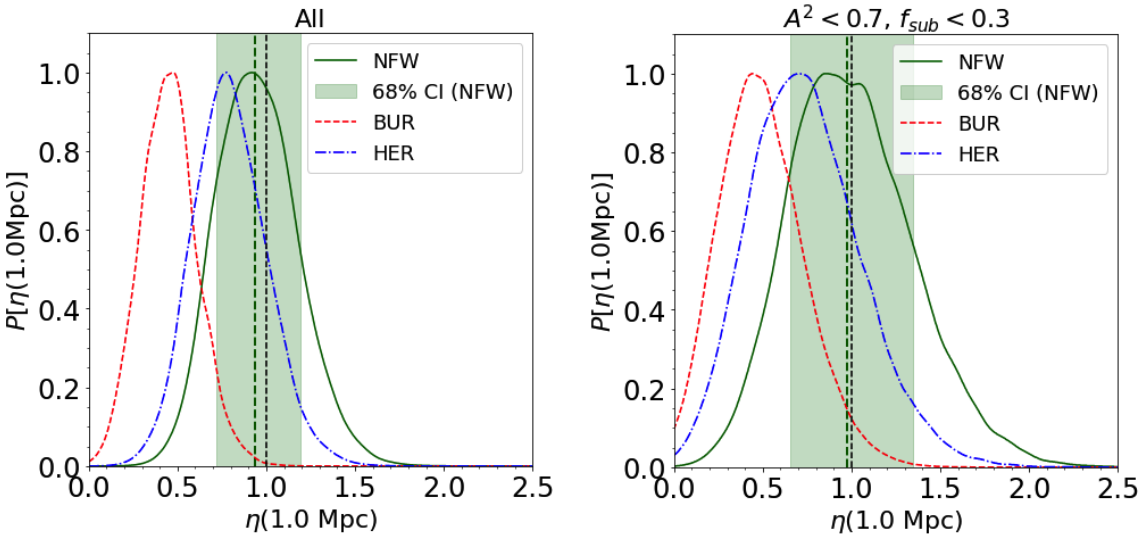

Figure 4. Left: posterior distributions of $\eta(r = 1.0\,\mathrm{Mpc})$ for the three mass models adopted in our analysis. The gT profile is assumed for the velocity anisotropy. Right: same, but considering only clusters with $A^2 < 0.6$ and $f_{sub} < 0.3$. In both plots, the dashed green vertical lines correspond to the median of the NFW-case distribution, and the green shaded regions indicate the corresponding $1\,\sigma$ confidence interval. The black short-dashed vertical lines indicate the "GR" value $\eta = 1$

The $\sim 3\sigma$ tension observed in the Burkert model can be explained again by inspecting the distributions $P(r_{200}, r_{-2})$ in figure 8. Compared to the NFW and Hernquist cases, the lensing analysis for the Burkert profile prefers overall lower values of r_{-2} and r_{200} for many clusters, with tighter constraints. From figure 4 of [22], it is clearly seen that when the Burkert profile is forced to fit the stacked lensing signal, it tends to favor the inner region where the signal-to-noise ratio is higher. As a consequence, the outer density profile is significantly underestimated. A similar bias may be present in individual cluster analyses, potentially explaining why both r_{200} and r_{-2} tend to be underestimated when modeling the lensing signal with a Burkert profile.

4.1 Impact of dynamical relaxation, offsets and velocity anisotropy

In order to establish the robustness of our analysis, let us consider the effect of departures from dynamical relaxation and the presence of substructures on the final constraints on η. As done in previous works (e.g. ref. [42, 57]), we adopt the Anderson-Darling coefficient A^2 of ref. [58], which quantifies deviation from Gaussianity of the line-of-sight velocity distribution, in order to estimate the magnitude of departures from dynamical equilibrium. The total fraction of galaxies in substructures, $f_{\rm sub}$, is further considered as a proxy for the disturbed state of clusters; for our sample, we use the values estimated in ref. [39], by running the DS+ algorithm of ref. [59], which combines the information of spatial distribution and line-of-sight velocity to detect subclusters. The values of $f_{\rm sub}$ and A^2 are listed in the last columns of table 1.

In figure 5, the constraints on $\eta(r = 1.0\,\mathrm{Mpc})$ as a function of A^2 (left) and $f_{\rm sub}$ (right) are shown for the NFW+gT model. By visually inspecting both plots, no strong evidences of correlation arise; moreover, when considering only the clusters with $A^2 < 0.7$ and $f_{\rm sub} < 0.3$,

JCAP03(2026)022

Cluster	NFW	Her	Bur
A383	$1.04^{+1.99}_{-1.11}$	$0.66^{+1.75}_{-0.92}$	$0.39^{+1.14}_{-0.72}$
A209	$1.09^{+1.29}_{-0.91}$	$0.87^{+1.14}_{-0.78}$	$0.76^{+0.84}_{-0.66}$
R2129	$0.51^{+1.45}_{-0.80}$	$0.36^{+1.41}_{-0.74}$	$0.07^{+0.86}_{-0.54}$
MS2137	$2.72^{+4.48}_{-2.46}$	$2.85^{+4.26}_{-2.45}$	$1.92^{+3.75}_{-2.19}$
R2248	$0.54^{+1.56}_{-0.82}$	$0.38^{+1.48}_{-0.77}$	$-0.08^{+0.82}_{-0.45}$
M1931	$1.89^{+3.82}_{-1.86}$	$1.67^{+3.50}_{-1.79}$	$0.67^{+2.29}_{-1.03}$
M1115	$1.81^{+1.92}_{-1.28}$	$1.87^{+1.73}_{-1.25}$	$1.53^{+1.56}_{-1.14}$
M1206	$1.65^{+1.66}_{-1.13}$	$1.45^{+1.57}_{-1.10}$	$0.98^{+1.21}_{-0.83}$
M329	$0.49^{+1.20}_{-0.74}$	$0.33^{+1.04}_{-0.64}$	$0.33^{+0.92}_{-0.61}$
Combined	$0.93^{+0.48}_{-0.40}$	$0.78^{+0.44}_{-0.38}$	$0.45^{+0.34}_{-0.30}$

Table 2. Constraints at $2\,\sigma$ on $\eta(r = 1.0\,\mathrm{Mpc})$ for each individual cluster, adopting the three mass models described in section 2, and for the combined distributions (last row).

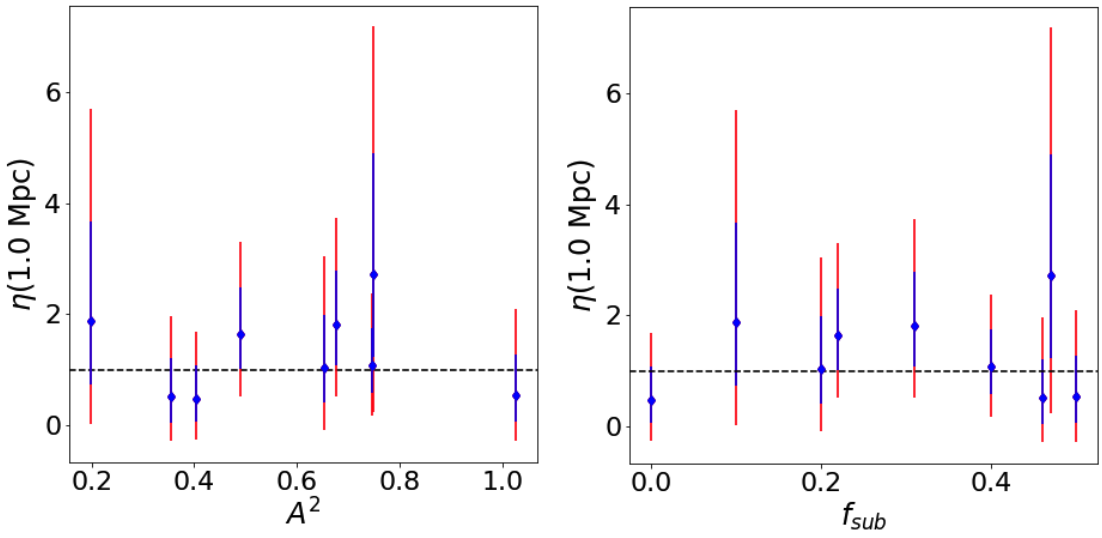

Figure 5. Constraints on $\eta(r = 1\,\mathrm{Mpc})$ for the NFW+gT reference case as a function of the Anderson-Darling coefficient A^2 on the left, and the fraction of galaxies in substructures f_{sub} on the right. The color code is as in figure 2.

namely M329, M1931, M1206 and A383, no substantial change in the combined distribution is found, as it can be seen in the left panel of figure 4.

JCAP03(2026)022

Note that the evidently un-relaxed cluster R2248 is indeed characterised by the largest value of both A^2 and $f_{\rm sub}$; thus the strong deviation of equilibrium may indeed produce the observed bias in the η distribution. However, for other cases (e.g. M329) while the criteria applied point towards a kinematic relaxation state, η exhibits a slight 1σ tension with the GR unity value. In this regard, it is worth pointing out that A^2 and $f_{\rm sub}$ are related to the kinematics of member galaxies only; other possible sources of systematics - such as projection effects or halo triaxiality - may have a stronger impact in the lensing mass profiles reconstruction (see e.g. [60]), explaining the trend $\eta \neq 1$ found for some clusters. As an example, the aforementioned foreground group in M1206 can contaminate the strong-lensing analysis by boosting the projected mass profile in the cluster core. In contrast, it has been excluded from the kinematic phase-space selection. This foreground contamination may therefore account for the discrepancy between the kinematic and lensing-based constraints on (r_{-2}, r_{200}). As discussed in ref. [43], adding the mass profile of the foreground group to the cluster mass profile obtained by MG-MAMPOSSt reproduces the lensing mass profile very well.

As an additional step, we discuss the impact of the velocity anisotropy profile model assumed in the kinematic analysis as well as of the variation of the lower limit of the projected radial range over which the kinematic data are considered in MG-MAMPOSSt, up to $R_{\rm min} = 0.2\,{\rm Mpc}$ (i.e. excluding the first 200 kpc), and down to $R_{\rm min} = 0\,{\rm Mpc}$. For the anisotropy ans'atz, besides the gT model, we run MG-MAMPOSSt with the BP profile of eq. (3.3); we also consider a third case where the usual assumption of $r_\beta = r_{-2}$ is adopted in the gT model. For each choice of the mass profile, we found that the resulting constraints are identical, independently of the model of $\beta(r)$, indicating that the choice of the model for the velocity anisotropy profile does not constitute a relevant source of systematics in this type of analysis. Similarly, the variation of the lower limit in the kinematic analysis does not provide significant variations in the final distributions of η. The posteriors obtained assuming different $\beta(r)$, and different values of $R_{\rm min}$ for the reference NFW mass case, are further reported in the left plot and right plot of figure 6, respectively.

A further potential source of systematic uncertainty is a mismatch between the centres adopted in the lensing and dynamical analyses. In our fiducial setup, both the kinematic analysis and the strong+weak lensing reconstruction are performed with respect to the position of the BCG. In the context of the CLASH sample, previous works (e.g., [49]) have shown that, for clusters selected as 'relaxed' by X-ray morphology, the BCG, the hot gas, and the lensing mass distributions are typically well aligned at scales of $\sim$500 kpc. However, more recent analyses (e.g. [61]) emphasise that projection effects and potential mis-centering can bias the reconstructed mass maps. They indicate that small projected offsets of order a few tens of kpc between the BCG, the X-ray peak, and the peak of the total mass distribution are not uncommon, especially in dynamically disturbed systems.

To quantify the impact of such offsets on our determination of $\eta(r)$, we performed a simple centering test at the level of the mass profiles. For each cluster and for each MCMC sample of the lensing posterior (r^L_{200}, r^L_s), we constructed a "mis-centred" lensing mass profile

$$M^{\rm off}_{\rm lens}(r\,|r^L_{200}, r^L_s) \equiv M_{\rm lens}\left(\sqrt{r^2 + R^2_{\rm off}}\,|r^L_{200}, r^L_s\right), \tag{4.2}$$

JCAP03(2026)022

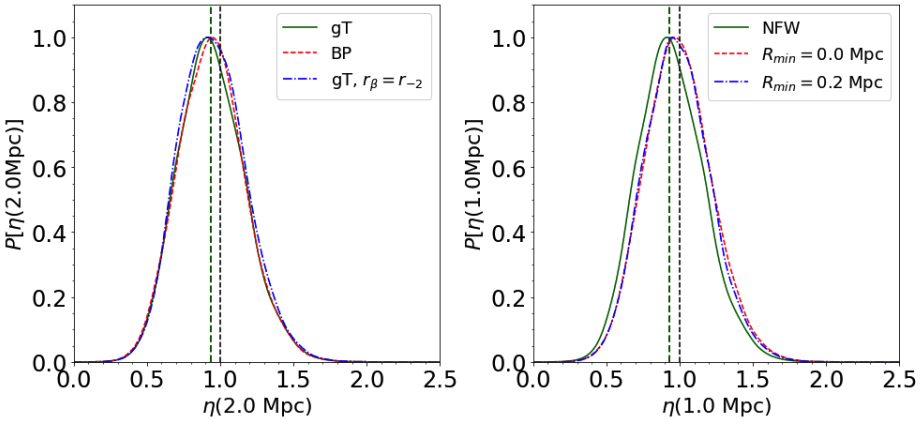

Figure 6. Left: posterior of $\eta(r = 1.0\,\mathrm{Mpc})$ for gT model of $\beta(r)$ (green solid), gT model with $r_\beta = r_{-2}$ (blue dash-dotted), and BP model (red dashed). The green vertical line is the mode of the gT-case distribution. The black short-dashed line is the GR expectation $\eta = 1$. Right: posteriors obtained varying $R_{\rm min}$ in the MG-MAMPOSSt fit to 0.2 (blue dash-dotted) and 0 (red dashed) Mpc. The green solid line is the same as the left plot. For all cases, the NFW mass model is assumed.

which approximates the suppression of the lensing signal when the tangential shear is measured around an incorrect centre displaced by a projected offset $R_{\rm off}$ from the true mass centroid. We considered values of $R_{\rm off} = 50$ and 100 kpc, which bracket the typical range of offsets measured between the BCG, X-ray, and lensing centroids in CLASH clusters (see, e.g., [22, 28]).

We then recomputed $\eta(r)$ by replacing $M_{\rm lens}(r)$ with $M^{\rm off}_{\rm lens}(r)$ in eq. (2.6), keeping the dynamical mass profiles unchanged. The resulting joint posterior distributions of $\eta(r = 1.0\,\mathrm{Mpc})$ are statistically indistinguishable from the fiducial case: the shift in the mode of the combined posterior is smaller than 0.05 for all the mass models, and remains well within the 1σ statistical uncertainty. This simple test shows that realistic centering offsets between lensing and kinematics do not constitute a dominant source of error in our analysis, and are effectively absorbed in our overall systematic error budget.

5 Conclusions

In this paper, we presented a parametric determination of the scale-dependent anisotropic stress $\eta(r) = \Psi(r)/\Phi(r)$ in the radial range $[0.1\,\mathrm{Mpc}, 1.2\,r^L_{200}]$. The term $\eta(r)$ is determined from the combination of kinematic and lensing mass profiles of nine massive galaxy clusters of the CLASH/CLASH-VLT sample. We used high-quality photometric and spectroscopic data of positions and line-of-sight velocities of member galaxies to jointly reconstruct the mass and velocity anisotropy profiles by means of the MG-MAMPOSSt code of ref. [21]. For different prescriptions for the mass profile models and the velocity anisotropy, we combined the kinematic mass with posteriors obtained by the strong+weak lensing analysis of ref. [22], allowing the constraint of $\eta(r)$.

For all clusters, when considering the Hernquist and NFW mass profiles, we found consistency with the expectation of GR ($\eta = 1$) within 2σ. For the Burkert model, two clusters show a quite strong ($\sim 3\sigma$) indication of $\eta \neq 1$; however, the Burkert profile is disfavored by the strong+weak lensing fit of ref. [22].

JCAP03(2026)022

No evidence of redshift evolution has emerged from our analysis, which allowed us to combine the posterior distributions of the anisotropic stress for each cluster, obtaining the constraint $\eta(r = 1.0\,\mathrm{Mpc}) = 0.93^{+0.22}_{-0.18}\,(1\sigma)\,^{+0.48}_{-0.40}\,(2\sigma) \pm 0.47\,(\mathrm{syst})$. The systematic encapsulates the effects of choosing different models for the lensing and kinematic mass profiles, while no variation induced by the choice of the anisotropy model has been found.

We further investigated possible relations between our results and the global degree of relaxation estimated from kinematical proxies, such as the Anderson-Darling coefficient, A^2, and the total fraction of galaxies in substructures f_{sub}. No strong indication of correlation was found; when further restricting the analysis to relaxed clusters with $A^2 < 0.7$ and $f_{\mathrm{sub}} < 0.3$, the joint constraints do not show significant changes.

The present analysis underscores two main findings. First, adopting the NFW model yields bounds on η that are approximately 40% tighter than previous determinations in the same redshift range - obtained from clusters (e.g. ref. [17]) -, and comparable to those from galaxy strong lensing (e.g. ref. [62]) or from combined probes such as CMB, weak lensing, and galaxy clustering (e.g. ref. [63]). The results are in agreement with theoretical predictions (e.g. ref. [23, 64, 65]). This confirms the constraining power of galaxy clusters as a test for signatures of non-standard models; crucially, this tool will become increasingly relevant in view of the large amount of imaging and spectroscopic data becoming available. Photometric surveys such as the Legacy Survey of Space and Time (LSST, e.g. ref. [66]), the *Euclid* satellite (e.g. ref. [67]) and the Nancy Grace Roman Space Telescope (e.g. ref. [68]) will not only provide deep and wide-field imaging, enabling weak lensing mass measurements for thousands clusters, but they will also detect over $\sim 10^5$ new galaxy clusters up to redshift $z \sim 2$ (e.g. ref. [69]). The discovery of such a vast population allows for the strict selection of large, statistically homogeneous samples of clusters over a vast range of cosmic history, which can be further stacked in fine bins of mass and redshift to average out projection or a-sphericity effects.

At the same time, spectroscopic campaigns, such as DESI (e.g. ref. [70]) and 4MOST (e.g. ref. [71]), will provide redshift and velocity measurements for tens of thousands of galaxies. These datasets will enable dynamical mass reconstruction and substructure analyses over large statistical samples of galaxy clusters, allowing to constrain the evolution of $\eta(r, z)$ with unprecedented statistical precision, of order of few percent. In parallel, dedicated cluster-focused surveys beyond CLASH, such as X-COP (e.g. ref. [72]), CHEX-MATE (e.g. ref. [73]), and HeCS/HeCS-SZ (e.g. ref. [74, 75]), offer detailed mass profile determinations down to the cluster core by combining multi-wavelength data (X-ray, SZ, and optical), providing stringent bounds on the dark sector and potential deviations from GR.

On the other hand, the mismatch observed between lensing and kinematic mass profiles in some clusters of the sample underscores the necessity of a thorough assessment and calibration of systematic uncertainties. Furthermore, it points to the importance of identifying reliable observational diagnostics - such as A^2 or f_{gas} - that can serve as selection criteria for a "golden sample" of galaxy clusters, suitable for deriving robust constraints on alternative theories of gravity. While here we have focused on kinematics mass profile reconstructions, similar criteria related to lensing and X-ray data should be derived, integrating those already existing in the literature in a full multi-probe atlas of systematic diagnostic.

JCAP03(2026)022

Note that for a few systems in our sample, such as M1206 or R2248, the availability of kinematic data of the BCG as well as the precise measurements of gas and stellar components allowed a more detailed mass profile determination down to $\sim$ 1 kpc (e.g. refs. [16, 43]). At the same time, refined strong lensing analysis has been performed to obtain the mass distribution in the core of M1206 (e.g. ref. [76]). This upgraded information will be used in future work to refine the single-cluster bounds on $\eta(r)$ as well as to get new insights on the behavior of gravity between astrophysical and cosmological scales.

A Kinematic vs lensing posteriors

In figures 7, 8, 9 we present the 1 σ and 2 σ regions in the space (r_{200}, r_{-2}) for the lensing (blue) and MG-MAMPOSSt kinematic (green) analyses. Each figure refers to a different choice of the model for the total cluster mass. Note that $r_{-2} = r_s/2$ for the Hernquist profile and $r_{-2} \simeq 3r_s/2$ for the Burkert profile.

While the kinematic analysis shows consistency among the three mass choices, the lensing results appear very different for the Burkert case (which, as mentioned in section 3, has been found to poorly fit the stacked lensing signal in [22]). Clusters as A209, M1115, R2248 exhibit a mild ($\lesssim 2\sigma$) tension between the lensing and kinematic distributions, which translates to a constrain on $\eta \neq 1$. Interestingly, the disagreement is reduced for A209 when the Burkert model is assumed. This can follow from the fact that A209 is the only galaxy cluster in the sample showing a core in the galaxy distribution (ref. [39]). On the contrary, the tension increases significantly in the case of R2248 and R2129 for the Burkert model.

Figure 10 further shows the radial mass profiles obtained from the lensing chains (blue solid line, blue shaded areas) and those resulting from the MG-MAMPOSSt pipeline (red). In all cases, we have assumed a NFW model.

B Radial profiles of $\eta(r)$

In figure 11 we plot the radial profiles of the anisotropic stress for the nine clusters in the sample, adopting a NFW+gT model. The darker and lighter shaded areas represent the 1 σ and 2 σ confidence region, respectively, while the median values are represented by the red solid line.

Acknowledgments

The authors acknowledge P. Rosati and the CLASH-VLT team for having provided the dataset used in this work. The authors further thank the anonymous Referee who provided valuable comments to improve the quality of the manuscript. K.U. acknowledges support from the National Science and Technology Council of Taiwan (grant NSTC 112-2112-M001-027-MY3) and the Academia Sinica Investigator Award (grant AS-IA112-M04). A. M. Pombo is supported by the Czech Grant Agency (GAČR) project PreCOG (Grant No. 24-10780S). This study is supported by the Italian Ministry for Research and University (MUR) under Grant 'Progetto Dipartimenti di Eccellenza 2023-2027' (BiCoQ).

JCAP03(2026)022

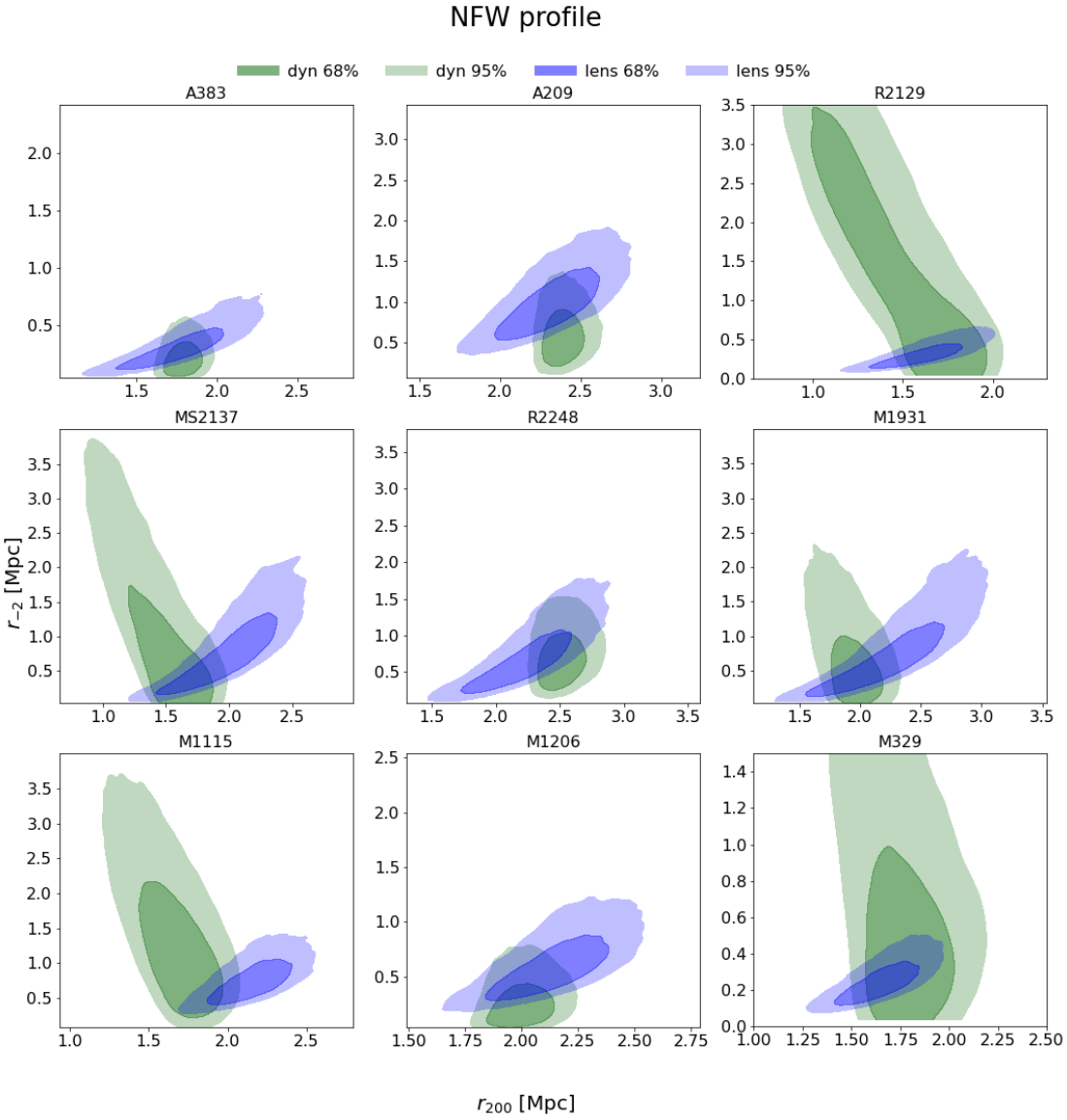

Figure 7. Two dimensional posterior distributions $P(r_{200}, r_{-2})$ at 1 σ (darker shaded regions) and 2 σ (lighter shaded regions) for the lensing and kinematic analyses of the nine CLASH clusters. The total mass is described by a NFW profile, and we adopted a gT model for the velocity anisotropy in the MG-MAMPOSSt fit. Blue: lensing. Green: kinematics.

JCAP03(2026)022

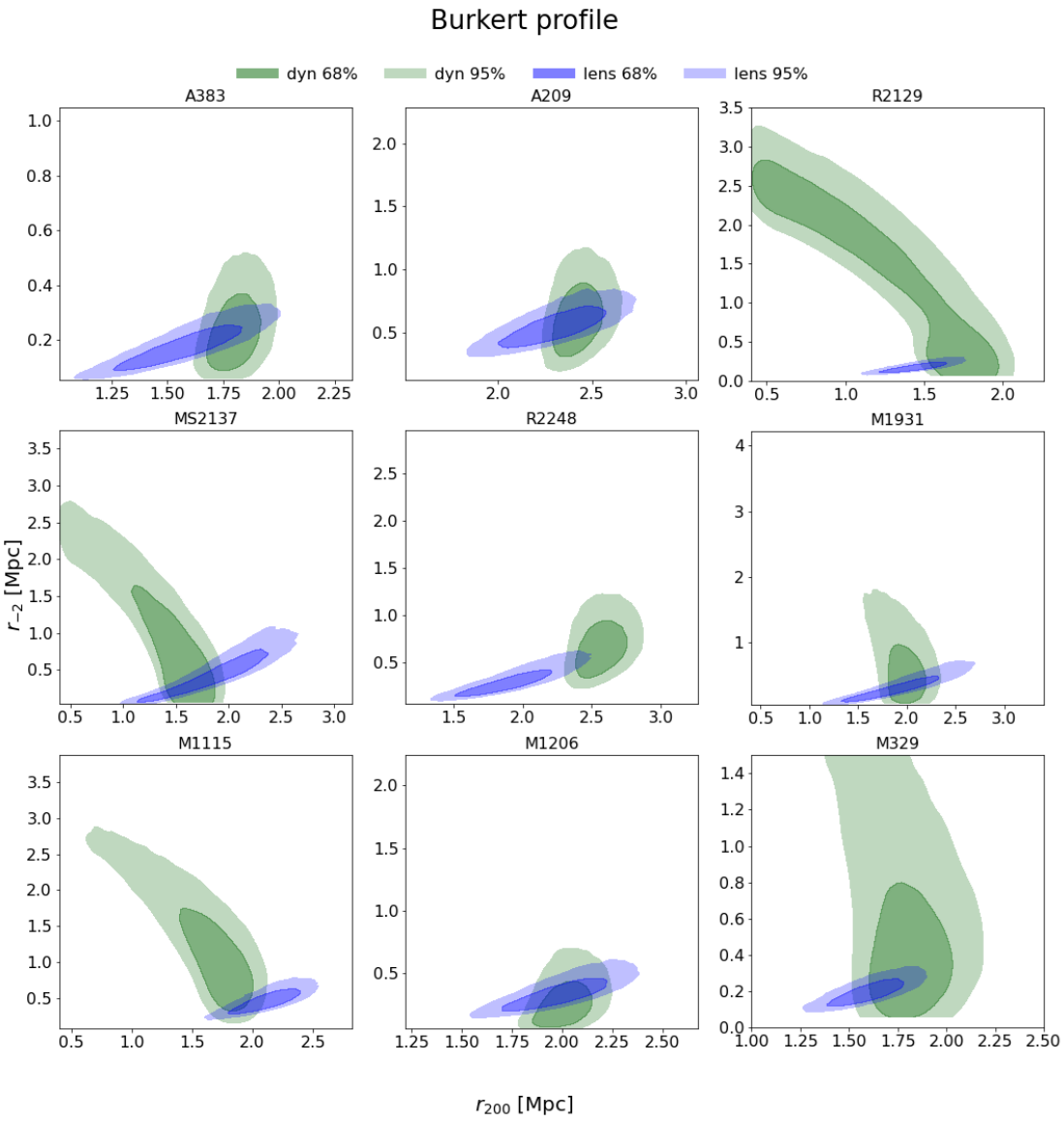

Figure 8. Same as figure 7 but for the Burkert model assumed for the total mass profile.

JCAP03(2026)022

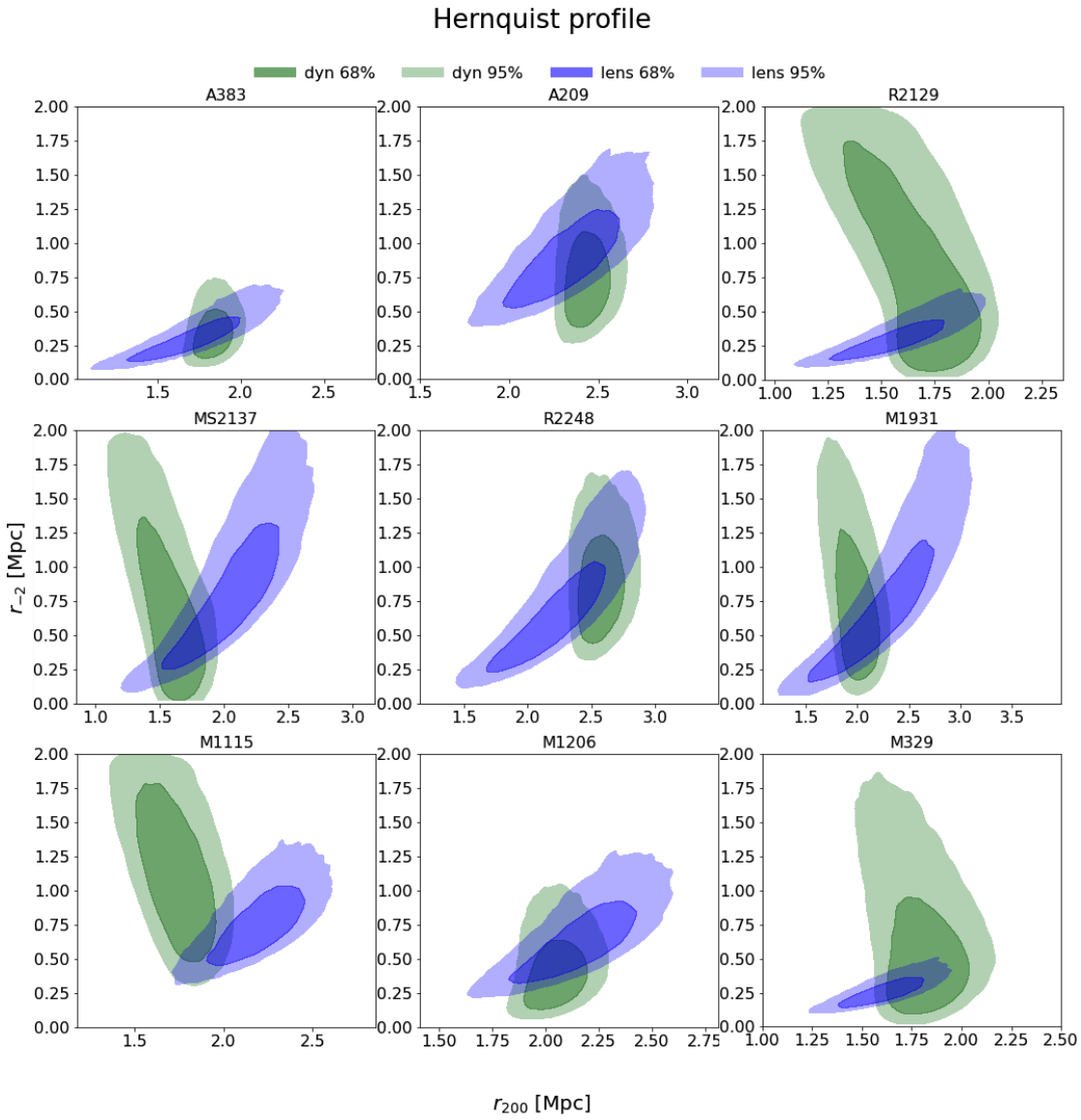

Figure 9. Same as figure 7 but for the Hernquist model assumed for the total mass profile.

JCAP03(2026)022

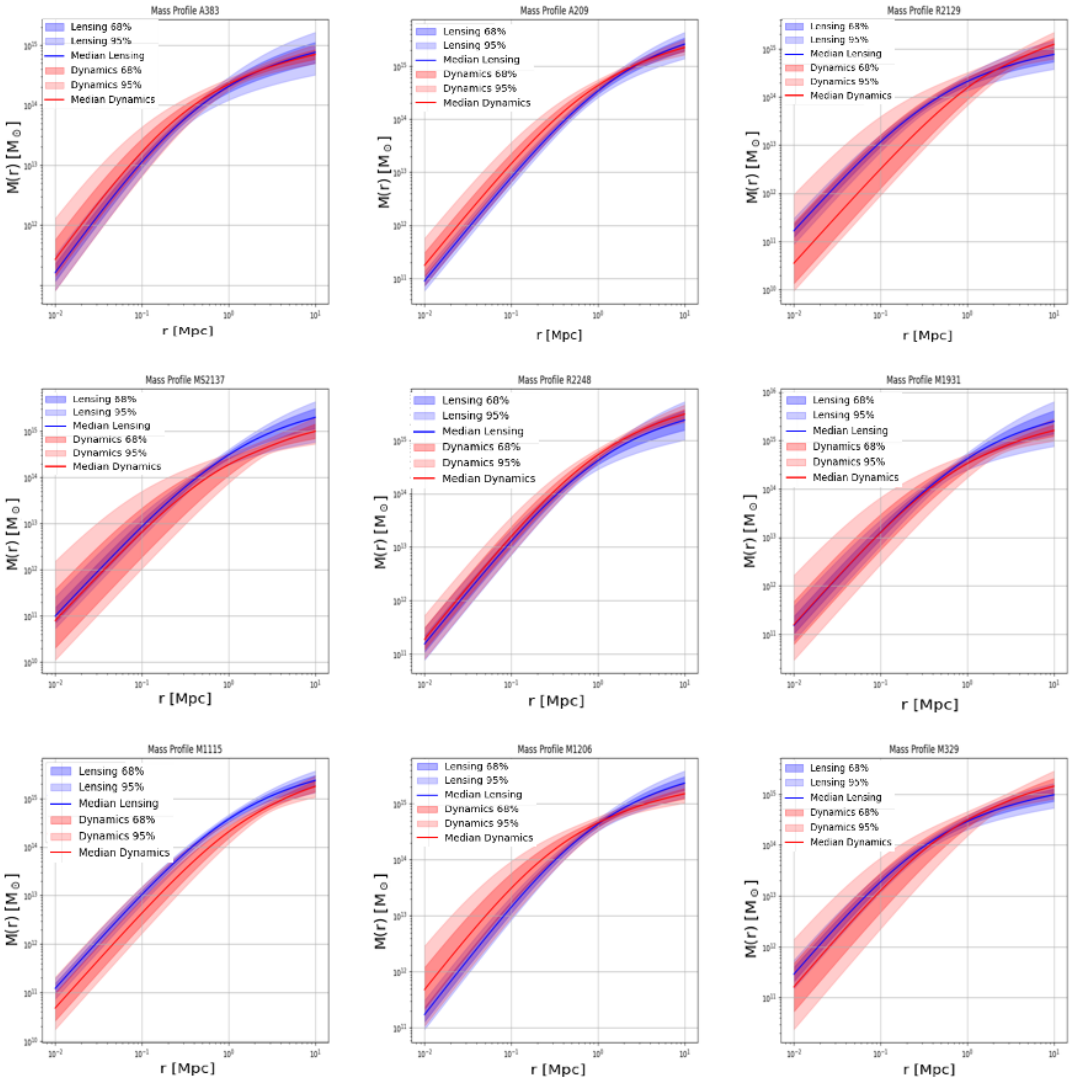

Figure 10. blue: strong+weak lensing radial mass profiles, in blue, compared to the mass profiles derived with MG-MAMPOSSt in red. The darker and lighter shaded regions indicate the 1σ and 2σ interval, respectively. Solid lines are the median profiles. All profiles are parametrised with the NFW model.

JCAP03(2026)022

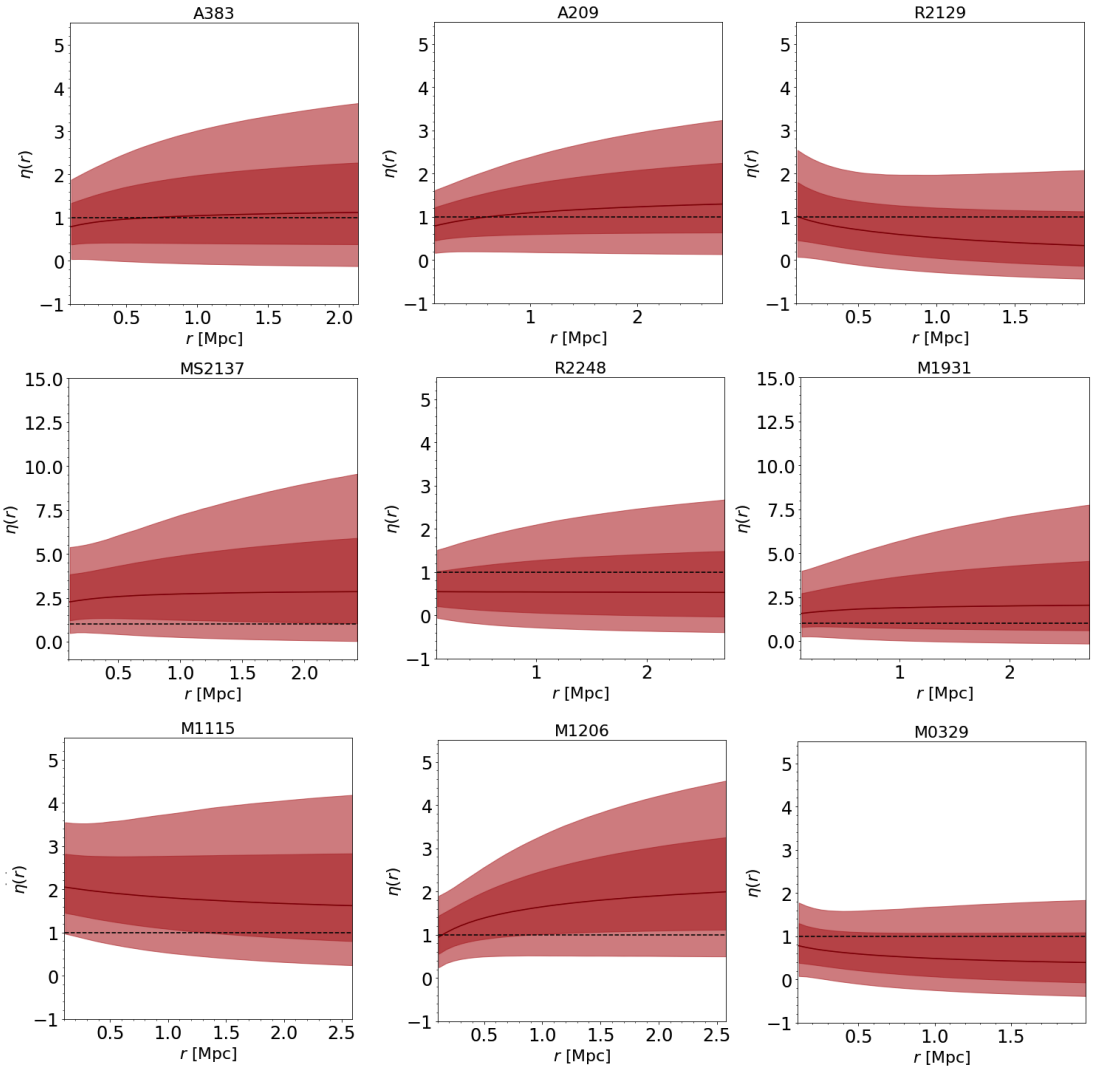

Figure 11. Radial profiles $\eta(r)$ obtained for the nine clusters in the sample adopting the reference model NFW+gT. In each plot, shaded regions refer to 1 σ (dark red) and 2 σ (light red) intervals; the red solid line indicates the median. The GR expectation $\eta = 1$ is marked by the horizontal black dashed line.

JCAP03(2026)022

References

[1] Supernova Search Team collaboration, *Observational evidence from supernovae for an accelerating universe and a cosmological constant*, *Astron. J.* **116** (1998) 1009 [astro-ph/9805201] [INSPIRE].

[2] Supernova Cosmology Project collaboration, *Measurements of Ω and Λ from 42 High Redshift Supernovae*, *Astrophys. J.* **517** (1999) 565 [astro-ph/9812133] [INSPIRE].

[3] L. Perivolaropoulos and F. Skara, *Challenges for ΛCDM: An update*, *New Astron. Rev.* **95** (2022) 101659 [arXiv:2105.05208] [INSPIRE].

[4] A. Padilla, *Lectures on the Cosmological Constant Problem*, arXiv:1502.05296 [INSPIRE].

[5] Foundational Aspects of Dark Energy (FADE) collaboration, *Modified Gravity Approaches to the Cosmological Constant Problem*, *Universe* **9** (2023) 63 [arXiv:2210.06810] [INSPIRE].

[6] DES collaboration, *Dark Energy Survey Year 3 results: Cosmological constraints from galaxy clustering and weak lensing*, *Phys. Rev. D* **105** (2022) 023520 [arXiv:2105.13549] [INSPIRE].

[7] M.A. Sabogal et al., *Quantifying the S8 tension and evidence for interacting dark energy from redshift-space distortion measurements*, *Phys. Rev. D* **110** (2024) 123508 [arXiv:2408.12403] [INSPIRE].

[8] D.J. Schwarz, C.J. Copi, D. Huterer and G.D. Starkman, *CMB Anomalies after Planck*, *Class. Quant. Grav.* **33** (2016) 184001 [arXiv:1510.07929] [INSPIRE].

[9] F.K. Hansen, E.F. Boero, H.E. Luparello and D.G. Lambas, *A possible common explanation for several cosmic microwave background (CMB) anomalies: A strong impact of nearby galaxies on observed large-scale CMB fluctuations*, *Astron. Astrophys.* **675** (2023) L7 [arXiv:2305.00268] [INSPIRE].

[10] J.-P. Hu and F.-Y. Wang, *Hubble Tension: The evidence of New Physics*, *Universe* **9** (2023) 94 [arXiv:2302.05709] [INSPIRE].

[11] E. Di Valentino et al., *In the realm of the Hubble tension—a review of solutions*, *Class. Quant. Grav.* **38** (2021) 153001 [arXiv:2103.01183] [INSPIRE].

[12] A.G. Riess et al., *A comprehensive Measurement of the Local Value of the Hubble Constant with 1 km s^{-1} Mpc^{-1} Uncertainty from the Hubble Space Telescope and the SH0ES Team*, *Astrophys. J. Lett.* **934** (2022) L7 [arXiv:2112.04510] [INSPIRE].

[13] DESI collaboration, *DESI 2024 VI: cosmological constraints from the measurements of baryon acoustic oscillations*, *JCAP* **02** (2025) 021 [arXiv:2404.03002] [INSPIRE].

[14] K. Koyama, *Cosmological Tests of Modified Gravity*, *Rept. Prog. Phys.* **79** (2016) 046902 [arXiv:1504.04623] [INSPIRE].

[15] A. Biviano and P. Salucci, *The radial profiles of the different mass components in galaxy clusters*, *Astron. Astrophys.* **452** (2006) 75 [astro-ph/0511309] [INSPIRE].

[16] B. Sartoris et al., *CLASH-VLT: a full dynamical reconstruction of the mass profile of Abell S1063 from 1 kpc out to the virial radius*, *Astron. Astrophys.* **637** (2020) A34 [arXiv:2003.08475] [INSPIRE].

[17] L. Pizzuti et al., *CLASH-VLT: Testing the Nature of Gravity with Galaxy Cluster Mass Profiles*, *JCAP* **04** (2016) 023 [arXiv:1602.03385] [INSPIRE].

JCAP03(2026)022

[18] S.M.L. Vogt et al., *Constraining f(R) gravity using future galaxy cluster abundance and weak-lensing mass calibration datasets*, *Phys. Rev. D* **109** (2024) 123503 [arXiv:2401.09959] [INSPIRE].

[19] M. Howard, A. Kosowsky and G. Valogiannis, *Galaxy Cluster Statistics in Modified Gravity Cosmologies*, arXiv:2205.13015 [INSPIRE].

[20] T. Anton, T. Clifton and D.B. Thomas, *Gravitational slip in the parameterized post-Newtonian cosmology*, *Class. Quant. Grav.* **42** (2025) 195018 [arXiv:2504.18479] [INSPIRE].

[21] L. Pizzuti, I.D. Saltas and L. Amendola, *mg-mamposst: a code to test modifications of gravity with internal kinematics and lensing analyses of galaxy clusters*, *Mon. Not. Roy. Astron. Soc.* **506** (2021) 595 [arXiv:2011.15089] [INSPIRE].

[22] K. Umetsu et al., *CLASH: Joint Analysis of Strong-Lensing, Weak-Lensing Shear and Magnification Data for 20 Galaxy Clusters*, *Astrophys. J.* **821** (2016) 116 [arXiv:1507.04385] [INSPIRE].

[23] L. Pizzuti et al., *Future constraints on the gravitational slip with the mass profiles of galaxy clusters*, *Mon. Not. Roy. Astron. Soc.* **486** (2019) 596 [arXiv:1901.01961] [INSPIRE].

[24] I. Tutusaus, C. Bonvin and N. Grimm, *Measurement of the Weyl potential evolution from the first three years of dark energy survey data*, *Nature Commun.* **15** (2024) 9295 [arXiv:2312.06434] [INSPIRE].

[25] J.F. Navarro, C.S. Frenk and S.D.M. White, *The structure of cold dark matter halos*, *Astrophys. J.* **462** (1996) 563 [astro-ph/9508025] [INSPIRE].

[26] A. Burkert, *The structure of dark matter halos in dwarf galaxies*, *Astrophys. J. Lett.* **447** (1995) L25 [astro-ph/9504041] [INSPIRE].

[27] L. Hernquist, *An analytical Model for Spherical Galaxies and Bulges*, *Astrophys. J.* **356** (1990) 359 [INSPIRE].

[28] M. Postman et al., *Cluster Lensing And Supernova survey with Hubble (CLASH): An overview*, *Astrophys. J. Suppl.* **199** (2012) 25 [arXiv:1106.3328] [INSPIRE].

[29] CLASH-VLT TEAM collaboration, *CLASH-VLT: A VIMOS Large Programme to Map the Dark Matter Mass Distribution in Galaxy Clusters and Probe Distant Lensed Galaxies*, *ESO Messenger* **158** (2014) 48 [INSPIRE].

[30] K. Umetsu et al., *The projected Dark and Baryonic Ellipsoidal Structure of 20 CLASH galaxy clusters*, *Astrophys. J.* **860** (2018) 104 [arXiv:1804.00664] [INSPIRE].

[31] K. Umetsu et al., *CLASH: Weak-Lensing Shear-and-Magnification Analysis of 20 Galaxy Clusters*, *Astrophys. J.* **795** (2014) 163 [arXiv:1404.1375] [INSPIRE].

[32] S. Miyazaki et al., *Subaru prime focus camera: Suprime-Cam*, *Publ. Astron. Soc. Jap.* **54** (2002) 833 [astro-ph/0211006] [INSPIRE].

[33] D. Gruen et al., *Weak lensing analysis of RXC J2248.7-4431*, *Mon. Not. Roy. Astron. Soc.* **432** (2013) 1455 [arXiv:1304.0764] [INSPIRE].

[34] O. LeFevre et al., *Commissioning and performances of the VLT-VIMOS*, in the proceedings of the *Instrument Design and Performance for Optical/Infrared Ground-based Telescopes*, Waikoloa, Hawaii, U.S.A., August, (2003) [DOI:10.1117/12.460959].

[35] R. Bacon et al., *The MUSE second-generation VLT instrument*, in the proceedings of the *Ground-based and Airborne Instrumentation for Astronomy III*, July (2010) [DOI:10.1117/12.856027] [arXiv:2211.16795].

JCAP03(2026)022

[36] K. Umetsu, *Cluster–galaxy weak lensing*, *Astron. Astrophys. Rev.* **28** (2020) 7 [arXiv:2007.00506] [INSPIRE].

[37] L. Pizzuti et al., *MG-MAMPOSSt, a Fortran code to test gravity at galaxy-cluster scales*, *J. Open Source Softw.* **8** (2023) 4800 [arXiv:2201.07194] [INSPIRE].

[38] G.A. Mamon, A. Biviano and G. Boue, *MAMPOSSt: Modelling Anisotropy and Mass Profiles of Observed Spherical Systems. I. Gaussian 3D velocities*, *Mon. Not. Roy. Astron. Soc.* **429** (2013) 3079 [arXiv:1212.1455] [INSPIRE].

[39] A. Biviano et al., *CLASH-VLT: The variance in the velocity anisotropy profiles of galaxy clusters*, arXiv:2508.05195 [INSPIRE].

[40] A. Biviano et al., *The GOGREEN survey: Internal dynamics of clusters of galaxies at redshift 0.9–1.4*, *Astron. Astrophys.* **650** (2021) A105 [arXiv:2104.01183] [INSPIRE].

[41] L. Pizzuti et al., *Testing refracted gravity with the kinematics of galaxy clusters*, *Astron. Astrophys.* **698** (2025) A83 [arXiv:2410.19698] [INSPIRE].

[42] L. Pizzuti et al., *CHEX-MATE: Exploring the kinematical properties of Planck galaxy clusters*, *Astron. Astrophys.* **699** (2025) A88 [arXiv:2505.03708] [INSPIRE].

[43] A. Biviano et al., *CLASH-VLT: The inner Slope of the MACS J1206.2-0847 Dark Matter Density Profile*, *Astrophys. J.* **958** (2023) 148 [arXiv:2307.06804] [INSPIRE].

[44] G.A. Mamon et al., *Structural and dynamical modeling of WINGS clusters. II. The orbital anisotropies of elliptical, spiral and lenticular galaxies*, *Astron. Astrophys.* **631** (2019) A131 [arXiv:1901.06393] [INSPIRE].

[45] A. Biviano et al., *The radial Orbits of Ram-pressure-stripped Galaxies in Clusters from the GASP Survey*, *Astrophys. J.* **965** (2024) 117 [arXiv:2403.02111] [INSPIRE].

[46] M. Bartelmann, *Arcs from a universal dark matter halo profile*, *Astron. Astrophys.* **313** (1996) 697 [astro-ph/9602053] [INSPIRE].

[47] I. King, *The structure of star clusters. I. An empirical density law*, *Astron. J.* **67** (1962) 471 [INSPIRE].

[48] C.L. Sarazin, *A maximum likelihood method for determining the distribution of galaxies in clusters*, *Astrophys. J.* **236** (1980) 75.

[49] M. Donahue et al., *The morphologies and Alignments of Gas, Mass, and the central Galaxies of CLASH Clusters of Galaxies*, *Astrophys. J.* **819** (2016) 36 [arXiv:1601.04947] [INSPIRE].

[50] Y. Jiménez-Teja et al., *Unveiling the Dynamical State of Massive Clusters through the ICL Fraction*, *Astrophys. J.* **857** (2018) 79.

[51] A. Mercurio et al., *CLASH-VLT: Abell S1063 - Cluster assembly history and spectroscopic catalogue*, *Astron. Astrophys.* **656** (2021) A147 [arXiv:2109.03305] [INSPIRE].

[52] A. Zitrin et al., *Hubble Space Telescope Combined Strong and Weak Lensing Analysis of the CLASH Sample: Mass and Magnification Models and Systematic Uncertainties*, *Astrophys. J.* **801** (2015) 44 [arXiv:1411.1414] [INSPIRE].

[53] M. Schaller et al., *The effect of baryons on the inner density profiles of rich clusters*, *Mon. Not. Roy. Astron. Soc.* **452** (2015) 343 [arXiv:1409.8297] [INSPIRE].

[54] S. Peirani et al., *Density profile of dark matter haloes and galaxies in the horizon–agn simulation: the impact of AGN feedback*, *Mon. Not. Roy. Astron. Soc.* **472** (2017) 2153 [arXiv:1611.09922] [INSPIRE].

JCAP03(2026)022

[55] S. Grandis et al., *Calibration of bias and scatter involved in cluster mass measurements using optical weak gravitational lensing*, *Mon. Not. Roy. Astron. Soc.* **507** (2021) 5671 [arXiv:2103.16212] [INSPIRE].

[56] L. Pizzuti et al., *Mass modeling and kinematics of galaxy clusters in modified gravity*, *JCAP* **11** (2024) 014 [arXiv:2407.08778] [INSPIRE].

[57] R. Barrena, L. Pizzuti, G. Chon and H. Böhringer, *Unveiling the shape: A multi-wavelength analysis of the galaxy clusters Abell 76 and Abell 1307*, *Astron. Astrophys.* **691** (2024) A135 [arXiv:2409.16981] [INSPIRE].

[58] T.W. Anderson and D.A. Darling, *Asymptotic Theory of Certain "Goodness of Fit" Criteria Based on Stochastic Processes*, *Annals Math. Statist.* **23** (1952) 193.

[59] J.A. Benavides, A. Biviano and M.G. Abadi, *DS+: A method for the identification of cluster substructures*, *Astron. Astrophys.* **669** (2023) A147 [arXiv:2212.00040].

[60] EUCLID collaboration, *Euclid preparation - LXVI. Impact of line-of-sight projections on the covariance between galaxy cluster multi-wavelength observable properties: insights from hydrodynamic simulations*, *Astron. Astrophys.* **695** (2025) A282 [arXiv:2412.00191] [INSPIRE].

[61] M. Muñoz-Echeverría et al., *Galaxy cluster mass bias from projected mass maps - THE THREE HUNDRED-NIKA2 LPSZ twin samples*, *Astron. Astrophys.* **682** (2024) A124 [arXiv:2305.14862] [INSPIRE].

[62] S. Guerrini and E. Mörtsell, *Probing a scale dependent gravitational slip with galaxy strong lensing systems*, *Phys. Rev. D* **109** (2024) 023533 [arXiv:2309.11915] [INSPIRE].

[63] J. Li and G.-B. Zhao, *Cosmological Tests of Gravity with the Latest Observations*, *Astrophys. J.* **871** (2019) 196 [arXiv:1806.05022] [INSPIRE].

[64] L. Amendola, G. Ballesteros and V. Pettorino, *Effects of modified gravity on B-mode polarization*, *Phys. Rev. D* **90** (2014) 043009 [arXiv:1405.7004] [INSPIRE].

[65] S. Casas et al., *Constraining gravity with synergies between radio and optical cosmological surveys*, *Phys. Dark Univ.* **39** (2023) 101151 [arXiv:2210.05705] [INSPIRE].

[66] K. Breivik et al., *From Data to Software to Science with the Rubin Observatory LSST*, arXiv:2208.02781.

[67] EUCLID collaboration, *Euclid. I. Overview of the Euclid mission*, *Astron. Astrophys.* **697** (2025) A1 [arXiv:2405.13491] [INSPIRE].

[68] L. Wenzl et al., *Cosmology with the Roman Space Telescope – Synergies with CMB lensing*, *Mon. Not. Roy. Astron. Soc.* **512** (2022) 5311 [arXiv:2112.07681] [INSPIRE].

[69] B. Sartoris et al., *Next Generation Cosmology: Constraints from the Euclid Galaxy Cluster Survey*, *Mon. Not. Roy. Astron. Soc.* **459** (2016) 1764 [arXiv:1505.02165] [INSPIRE].

[70] DESI collaboration, *The DESI Experiment Part I: Science,Targeting, and Survey Design*, arXiv:1611.00036 [INSPIRE].

[71] R.S. de Jong et al., *4MOST: Project overview and information for the First Call for Proposals*, arXiv:1903.02464 [DOI:10.18727/0722-6691/5117].

[72] D. Eckert et al., *The XMM cluster outskirts project (X-COP)*, *Astron. Nachr.* **338** (2017) 293 [arXiv:1611.05051] [INSPIRE].

[73] CHEX-MATE collaboration, *The Cluster HEritage project with XMM-Newton: Mass Assembly and Thermodynamics at the Endpoint of structure formation - I. Programme overview*, *Astron. Astrophys.* **650** (2021) A104 [arXiv:2010.11972] [INSPIRE].

JCAP03(2026)022

[74] K. Rines, M.J. Geller, A. Diaferio and M.J. Kurtz, *Measuring the Ultimate Mass of Galaxy Clusters: Redshifts and Mass Profiles from the Hectospec Cluster Survey (HeCS)*, *Astrophys. J.* **767** (2013) 15 [arXiv:1209.3786] [INSPIRE].

[75] K.J. Rines, M.J. Geller, A. Diaferio and H.S. Hwang, *HeCS-SZ: The hectospec Survey of Sunyaev-Zeldovich Selected Clusters*, *Astrophys. J.* **819** (2016) 63 [arXiv:1507.08289] [INSPIRE].

[76] P. Bergamini et al., *New high-precision strong lensing modeling of Abell 2744 - Preparing for JWST observations*, *Astron. Astrophys.* **670** (2023) A60 [arXiv:2207.09416] [INSPIRE].

JCAP03(2026)022